Journal of Nuclear Materials 557 (2021) 153280

Contents lists available at ScienceDirect

Journal of Nuclear Materials

journal homepage: www.elsevier.com/locate/jnucmat

# Understanding the local thermal conductivity evolution of neutron irradiated $U_3Si_2$ dispersion fuel via state-of-the-art thermo-reflectance measurements

T.R. Pavlov[a,*], S.C. Middlemas[a], B.D. Miller[a], F. Cappia[a], J.I. Cole[b], J.J. Giglio[a]

[a] Idaho National Laboratory, Characterization and Advanced PIE Division, P.O. Box 1625, Idaho Falls, ID 83415, USA
[b] Idaho National Laboratory, Nuclear Fuels and Materials Division, P.O. Box 1625, Idaho Falls, ID 83415, USA

ARTICLE INFO

*Article history:*
Received 1 March 2021
Revised 12 July 2021
Accepted 31 August 2021
Available online 3 September 2021

*Keywords:*
Intermetallic
Composite
Amorphization
Thermal analysis
Irradiation
$U_3Si_2$

ABSTRACT

This study presents the first thermal conductivity measurements performed on neutron irradiated $U_3Si_2$ dispersion fuel cladded in an aluminum matrix (in a plate geometry). These were performed via a novel set-up which consists of a thermo-reflectance apparatus, known as the thermal conductivity microscope (TCM), deployed in a shielded glovebox. Thermal conductivity was measured across different fuel particles at various positions along the plate length and correlated to the local burnup. Back scattered electron images were collected at each position and analyzed to obtain estimates of the local porosity. It was shown that the thermal conductivity of the irradiated fuel particles is approximately 25% to 35% lower compared to the unirradiated material. A solid-state physics model was used to interpret the measured data. According to the model the degradation in thermal conductivity is consistent with the presence of insulating, fission gas filled pores or bubbles as well as loss of long-range order due to irradiation induced amorphization.



## 1. Introduction

The Material management and Minimization (M3) program aims to enable the conversion of research and test reactors fueled with highly enriched uranium (HEU) to low-enriched uranium (LEU) nuclear fuels [1,2]. One of the main requirements of these LEU conversion fuels is the need for fuel cores with high uranium density [3]. Pure uranium metal has been shown unsuitable due to its dimensional instability during irradiation [4]. This has prompted research into various alloys and compounds of uranium – uranium nitrides [5], uranium aluminates [6,7], uranium molybdates [8,9] and uranium silicides [10,11].

The U-Si phase diagram exhibits six intermetallic phases - $U_3Si$, $U_3Si_2$, USi, $U_3Si_5$, $USi_{1.88}$ and $USi_3$. Initially the $U_3Si$ system attracted significant research attention by having the highest fissile element density [12]. However, its breakaway swelling has proven life limiting [13]. $U_3Si$ exhibits a lower fraction of the stronger Si-Si bonds compared to $U_3Si_2$. This difference in bonding is considered to be the driving force for the higher viscosity [14], enhanced fission gas retention and lower swelling characteristic of $U_3Si_2$. As a result, $U_3Si_2$ is the only qualified high density LEU fuel and has been successfully used to convert around 60% of research reactor fuel from HEU to LEU [15]. These fuels typically have a plate geometry [15,16], a schematic of which is shown in Fig. 1. Thus, a central fuel zone is encapsulated by a cladding material (typically this is an aluminum alloy). Amongst the most important properties which is needed for the qualification and licensing of these fuels in high power compact cores is the thermal conductivity which is crucial for predicting the temperature of the fuel during reactor operation and, thus, establishing the fuel's ability to eject heat. Various authors have reported this property for unirradiated $U_3Si_2$ [17], however, to the authors knowledge, no post-irradiated measurements exist of the thermal conductivity of $U_3Si_2$. In this context, the current study will provide the first thermal conductivity measurements performed on irradiated $U_3Si_2$ dispersion fuel. These measurements are performed locally (with a resolution of approximately 50 $\mu$m) via a state-of-the-art thermo-reflectance technique [18,19] specifically designed and deployed for measurements of highly radioactive materials [20].

## 2. Methodology

### 2.1. Sample description and preparation

The sample was prepared from the U0R060 mini-plates. These were irradiated for two cycles in the top part of the RERTR-8 ex-

* Corresponding author.
*E-mail address:* tsvetoslav.pavlov@inl.gov (T.R. Pavlov).

https://doi.org/10.1016/j.jnucmat.2021.153280
0022-3115/

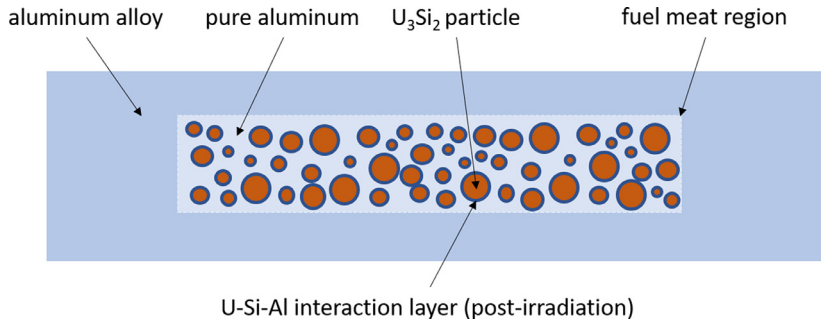


**Fig. 1.** Schematic of a $U_3Si_2$ dispersion fuel plate cross-section. The arrows point to the different regions and materials in the plate.

periment assembly in the Advanced Test Reactor (ATR) at Idaho National Laboratory (INL). The end of cycle fission power densities for the first and second cycles were 6773 W $cm^{-3}$ and 4923 W $cm^{-3}$, respectively. The maximum plate surface temperatures during the first and second cycles were calculated to be 368.8 K and 358.3 K, respectively. Further details on the irradiation parameters can be found elsewhere [21,22]. The local fuel fission density was calculated from the average plate fission density, the fuel to matrix volume ratio and adjusted via the interpolated radial and axial local to average neutron flux ratios (all of this information can be found elsewhere [21]). The samples were sectioned alongside the length of the fuel plate using a low speed saw. The open surface resulting from the cut was then polished to a 1 $\mu$m surface finish.

### 2.2. Scanning electron microscopy (SEM) and image analysis

Back scattered electron (BSE) images were collected using a FEI HELIOS NANOLAB 600 Dual Beam FIB/SEM. The sample surface was mapped using a series of BSE images at 500x magnification. Image segmentation was applied without any prior pre-processing. The segmentation is based on image gray-scale clustering. The built-in MATLAB k-means clustering algorithm was used to classify the objects in the image into three groups: background, fuel meat and porosity. Once the segmentation was completed, the user could select a desired location on the image. The chosen coordinates determine the center of a circle on the image with a user specified radius (in pixel units). Subsequently, the fraction of the porous phases is determined within the bounds of the specified circular area. The porosity is evaluated by calculating the ratio between pixels characteristic of the porous phase and the total number pixels bounded within the specified circle. The relative error on the porosity was obtained by assuming two standard deviations between values of porosity obtained from images at magnifications of 500x and 2500x, respectively.

### 2.3. Thermal conductivity microscope (TCM)

The TCM layout is shown in Fig. 2. The sample is potted in a metallographic mount and polished to a high-quality surface finish. The polished sample is then sputter coated alongside a transparent borosilicate crown glass (BK7) sample. The BK7 gold film thickness is measured via an in-house developed laser device [23]. Gold's reflectivity is very sensitive to temperature changes at around 532 nm (high coefficient of thermo-reflectance in absolute terms) which makes it a good candidate for probing the temperature response along the sample surface. The pump and probe are continuous wave lasers which operate at 660nm and 532 nm, respectively. The pump laser, as the name suggests, serves as a periodic heat source which is subjected to sinusoidal modulation via a function generator. The pump laser light is passed through a set of lenses, reflected off a short-pass dichroic mirror and focused via an objective onto the sample surface. The probe laser beam is p-polarized via a half-wave plate and transmitted through a polarizing beam splitting (PBS) cube. It is then reflected via a long-pass mirror, circularly polarized via a quarter-wave plate, and focused onto to the gold-coated sample surface. The reflected probe beam is, then, passed again through the quarter-wave plate and transformed into s-polarized light. It is reflected off the long-pass mirror and then reflected by the PBS onto the photodetector. The voltage reading produced by the photodetector is passed through a pre-amplifier and, finally, the periodic thermal response signal is extracted via a lock-in amplifier. The pump laser is initially focused away from the probe. It is, then, incrementally moved towards the probe beam until they become coincidental. At every location the thermal response measured by the detector is recorded and a phase difference between the reference (pump) and detected (probe) phases is calculated. This process is repeated at different separation distances between the pump and the probe lasers and at a range of modulation frequencies (1kHz to 100kHz). The probe beam is scanned using a pair of Newport VP-25XA stages and a Newport ESP301 controller. The phase difference is simultaneously calculated via a numerical solution to the three dimensional, two-layer transient heat transfer problem [18]. An optimization algorithm is employed to determine thermal diffusivity and thermal conductivity by minimizing the least squares difference between the model output and experimental data. The method and equipment has been previously extensively tested on standard reference materials such as $CaF_2$, ZnS, ZnSe and fused $SiO_2$ [19,24].

### 2.4. Condensed matter analysis

This section outlines the theoretical framework behind the solid-state physics models which were implemented in this work to interpret the measured experimental data. These models were used to calculate thermal conductivity, specific heat and thermal diffusivity of fresh and irradiated $U_3Si_2$. A detailed description the models can be found in the Appendix.

#### 2.4.1. Thermal conductivity

$U_3Si_2$ is a metallic material with free electrons in a partially filled conduction band. Thus, the material's thermal conductivity can be expressed as a sum of lattice ($k_l$) and electronic ($k_{el}$) components [25,26] (please refer to section A1 in the Appendix for a detailed description of $k_l$ and $k_{el}$) :

$$k_{tot} = k_l + k_{el} \tag{1}$$

The nuclear fission process leads to the splitting of uranium atoms into a distribution of possible new elements known as the yield curve. Certain elements such as Xe are nearly insoluble in the fuel matrix and precipitate in the form of bubbles [27]. These can be treated as a thermally insulating second phase in the $U_3Si_2$ fuel. Thus, to account for the effect of bubbles the Maxwell-Eucken

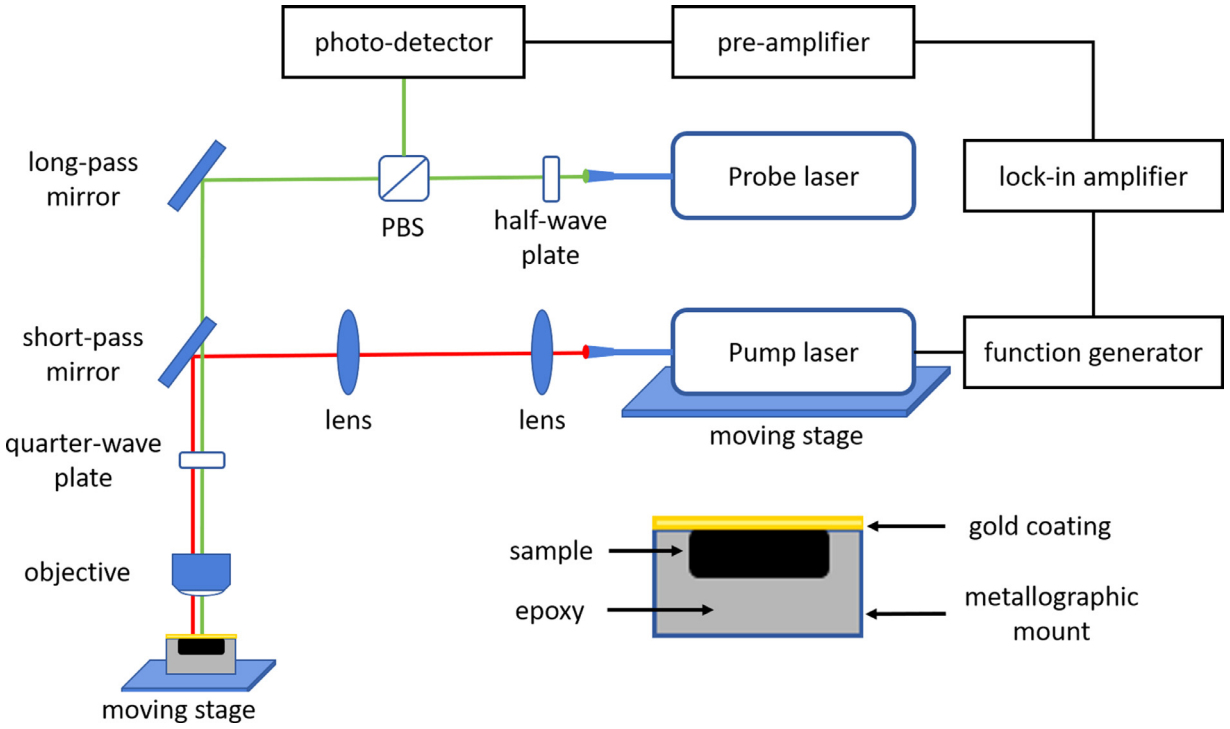


**Fig. 2.** Experimental layout of the thermal conductivity microscope.

relationship is applied [28]:

$$k_{eff} = k_1 \frac{2k_1 + k_2 - 2(k_1 - k_2)(1 - v_2)}{2k_1 + k_2 + (k_1 - k_2)(1 - v_2)} \quad (2)$$

where $k_{eff}$ is the effective thermal conductivity, $k_1$ is the thermal conductivity of the $U_3Si_2$ fuel matrix ($k_1$ is equivalent to $k_{tot}$ from Eq. (1), $k_2$ is the thermal conductivity of the bubbles, $v_1$ and $v_2$ are the phase fractions of the $U_3Si_2$ fuel and the bubbles (gas filled pores), respectively. Porosity has been varied between 0% and 15% in the thermal conductivity model (Eq. (1) and Eq. (2)) and the calculated values are compared to this work's measured (irradiated) and literature (as fabricated) data sets (see Fig. 4).

*2.4.2. Specific heat*

The molar specific heat of a metallic solid can be expressed by the sum of the following terms [29,30]:

$$c_P^{tot} = c_V^h + c_V^{el} + c_P^d + c_{V\to P}^{ah} \quad (3)$$

where $c_V^h$ is the harmonic contribution due to phonons, $c_V^{el}$ is the electronic contribution due to free electrons, $c_P^d$ is the contribution due to defects and $c_{V\to P}^{ah}$ is the constant volume to constant pressure conversion term. For the purpose of the current study the calculations will be confined to room temperature and, thus, it will be approximated that $c_P^d = 0$ and $c_{V\to P}^h = 0$ (please refer to section A2 in the Appendix for a detailed description of $c_V^h$ and $c_V^{el}$)

*2.4.3. Thermal diffusivity*

The thermal diffusivity ($\alpha$) is expressed as a function of the calculated thermal conductivity ($k$), specific heat ($c_P$) and the measured density ($\rho$) (all of which are also computed as a function of porosity):

$$\alpha = \frac{k}{\rho c_P} \quad (4)$$

The input parameters and constants for the model are summarized in Table 1.

## 3. Results

The microstructure of the $U_3Si_2$ fuel plate has been mapped and is shown in Fig. 3. Fig. 3A to 3F show enlarged sections of an SEM map containing the locations at which thermal conductivity and thermal diffusivity measurements were performed. The SEM BSE images (contrast dependent on elemental composition) show the fuel particles in light colors consistent with the presence of the heavy element uranium. The dark regions represent the aluminum matrix in which the particles are embedded. On the border of the particles thin regions exist which exhibit intermediate contrast between the light particles and dark matrix. These are characteristic of the U-Si-Al interaction layer.

The measurements of local thermal diffusivity and thermal conductivity are presented alongside local porosity and fission density in Table 2. The locations A to F in Table 2 correspond to Fig. 3A to Fig. 3F. The fission densities correspond to burnups between 13% FIMA and 18% FIMA with a plate average of approximately 15% FIMA. The specific heat values have been derived from the thermal conductivity, thermal diffusivity, and density (obtained by correcting for local porosity). The error of specific heat has been obtained by applying the error propagation law.

The measured thermal conductivity is presented as a function of local porosity in Fig. 4A. The measurements are compared to the values reported by White et al. [17] and Antonio et al. [31] as well as the model presented in this work. The agreement between the model results and the various experimental data sets is acceptable. The measurements on the irradiated sample show significantly lower values compared to unirradiated $U_3Si_2$. Fig. 4B shows thermal conductivity as a function of fission density. It is evident that thermal conductivity decreases both with increasing porosity and increasing fission density.

The evolution of the measured thermal diffusivity as a function of the local porosity is shown in Fig. 5A. The new measurements are compared to the thermal diffusivity obtained from Antonio et al. [31] and the model developed in the current study. The model is in good agreement with the irradiated results, how-

**Table 1**
List of model input parameters.

| Parameter | Units | Symbol | Value | Reference |
|---|---|---|---|---|
| Debye temperature | K | $\vartheta$ | 250 | *** |
| Electrical conductivity of $U_3Si_2$* | $m\Omega^{-1}$ $m^{-1}$ | $\sigma_1$ | 8.38 | [31] |
| Effective electron mass | $m_e$** | $m^*$ | 1 | *** |
| Fermi level | eV | $E_f$ | 4.5 | *** |
| Thermal conductivity of $U_3Si_2$* | W $m^{-1}$ $K^{-1}$ | $k_1$ | 8.8 | [31] |
| Thermal conductivity of pore phase | W $m^{-1}$ $K^{-1}$ | $k_2$ | 0.02 | *** |
| Theoretical density of $U_3Si_2$* | kg $m^{-3}$ | $\rho$ | 12 200 | [17,31] |
| *at 298 K and extrapolated to 100% TD | | | | |
| ** multiples of $m_e=9.11\times10^{-31}$ | | | | |
| *** value recommended in this work | | | | |

**Table 2**
Table of measured properties and characteristics for each of the locations in Fig. 3. The fission density is reported per volume of fuel. Errors are based on two standard deviations. All errors represent a single standard deviation.

| location | fission density (fissions $cm^{-3}$) | specific heat (J $kg^{-1}$ $K^{-1}$) | thermal diffusivity ($mm^2$ $s^{-1}$) | diffusivity error ($mm^2$ $s^{-1}$) | porosity(-) | thermal conductivity (W $m^{-1}$ $K^{-1}$) | conductivity error (W $m^{-1}$ $K^{-1}$) |
|---|---|---|---|---|---|---|---|
| A1 | 4.92 | 167.3 | 3.080 | 0.1160 | 0.114 | 5.615 | 0.784 |
| B1 | 4.33 | 179.1 | 3.270 | 0.1720 | 0.100 | 6.480 | 0.758 |
| B2 | 4.25 | 148.8 | 3.530 | 0.1220 | 0.093 | 5.860 | 0.423 |
| C1 | 4.01 | 156.5 | 3.207 | 0.1270 | 0.110 | 5.495 | 0.251 |
| D1 | 3.93 | 168.8 | 3.437 | 0.1650 | 0.101 | 6.416 | 0.373 |
| E1 | 3.83 | 155.6 | 3.409 | 0.2030 | 0.110 | 5.808 | 1.166 |
| F1 | 3.61 | 172.4 | 3.270 | 0.1010 | 0.119 | 6.110 | 0.480 |

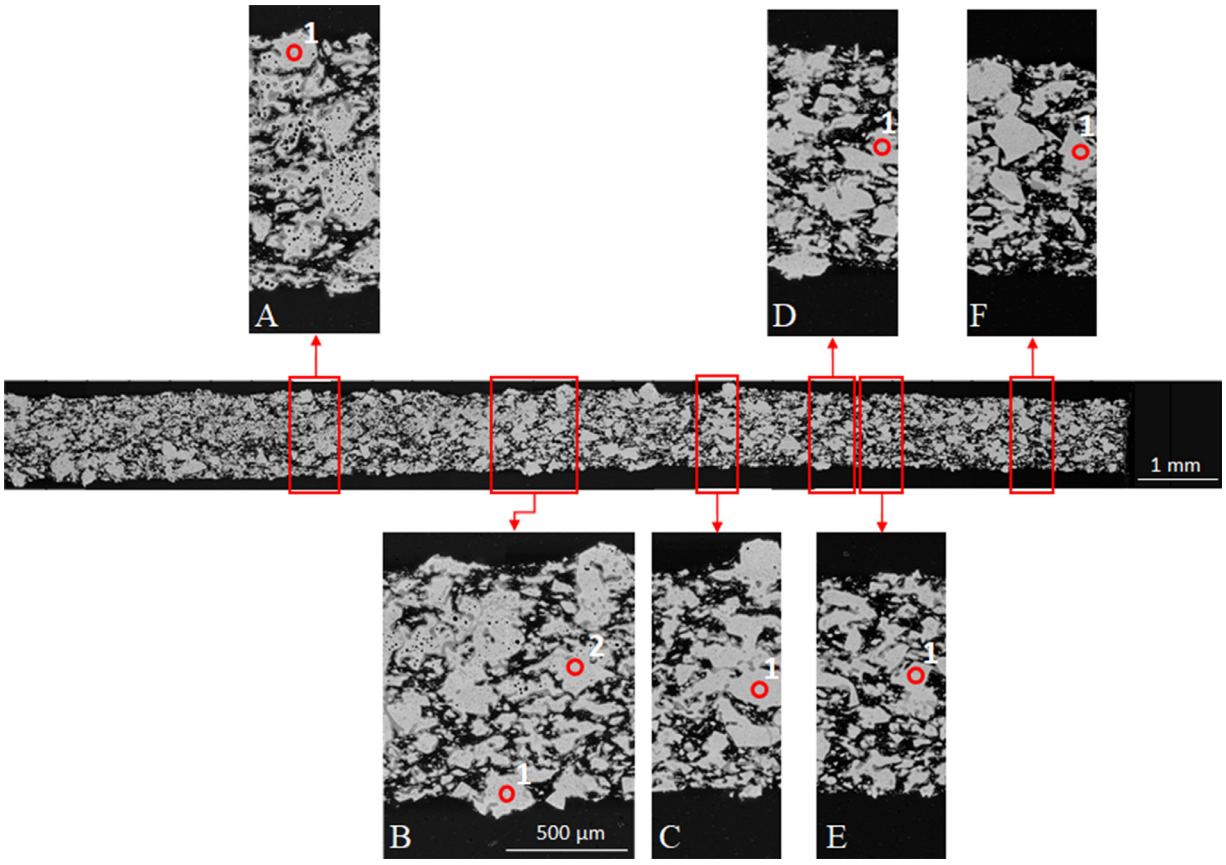


**Fig. 3.** A secondary electron image of a cross section of a $U_3Si_2$ fuel plate. Sections (A) to (F) show the locations at which local thermal conductivity measurements were performed. The subFig.s (A) to (F)have the same magnification (500x) while the central image has a lower magnification (50x).

ever, it predicts higher thermal diffusivity values when compared to the literature values for the unirradiated material. Fig. 5B shows the evolution of thermal diffusivity as a function of fission density. Similarly, to thermal conductivity, thermal diffusivity degrades with increases in porosity and fission density.

The specific heat results determined in this work are presented as a function of the local fission density in Fig. 6. The new data is compared to various measurements reported in the open literature – Mohamad et al. [32], White et al. [17] Cape and Taylor [33], Knacke et al. [34]. Furthermore, all results are compared

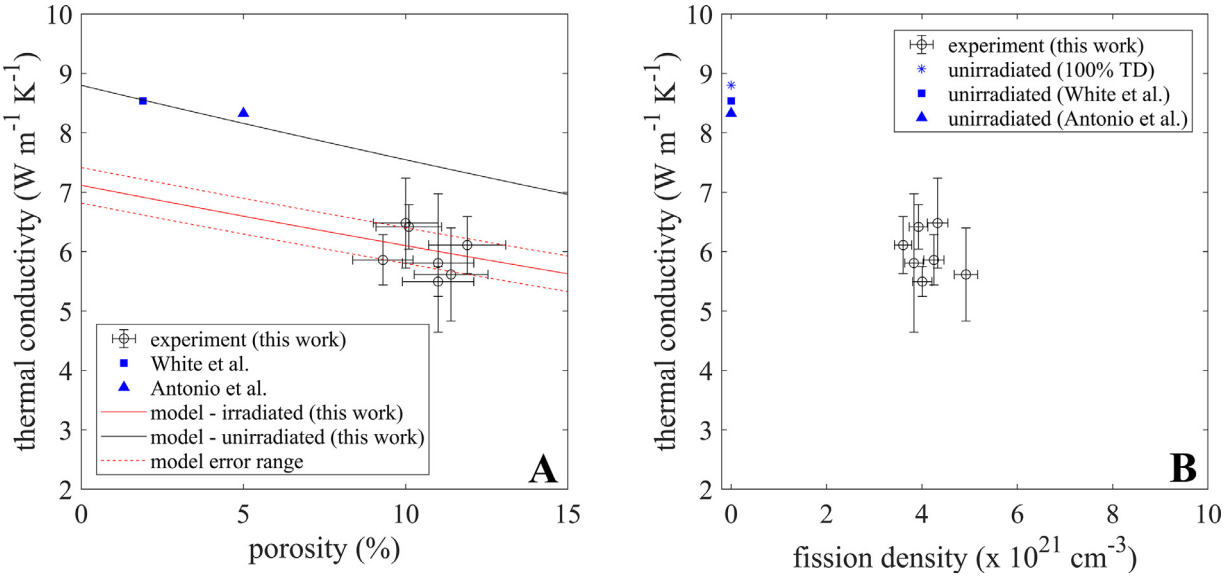


**Fig. 4.** Local thermal conductivity measurements of the irradiated $U_3Si_2$ fuel particles at room temperature. A) Thermal conductivty plotted as a function of porosity. The irradiated measuremetns in this work are compared to literature data on fresh $U_3Si_2$ at room temperature (White et al. [17] and Antonio et al. [31]) and to the model prediction. B) Thermal conductivty plotted as a function of fission density. The irradiated measuremetns in this work are compared to literature data on fresh U3Si2 (White et al. [17] and Antonio, [31]) as well as the value for fresh $U_3Si_2$ extrapolated to 100% TD. The fission density is reported per volume of fuel. All error bars represent a single standard deviation.

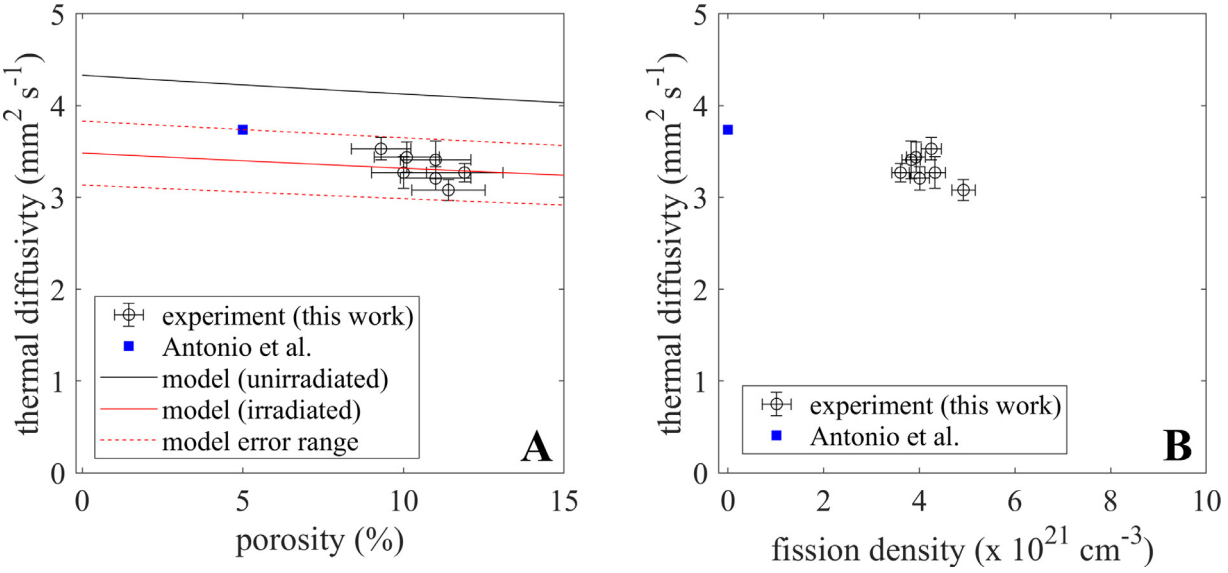


**Fig. 5.** Local thermal diffusivity measurements of the irradiated $U_3Si_2$ fuel particles at room temperature. A) Thermal diffusivity plotted as a function of porosity. The irradiated measuremetns in this work are compared to the model prediction. B) Thermal diffusivity plotted as a function of fission density. The irradiated measuremetns in this work are compared to literature data on fresh $U_3Si_2$ (calculated from specific heat and thermal conductivity obtained from Antonio et al. [31]). The fission density is reported per volume of fuel. All errors represent a single standard deviation.

to the theoretical harmonic limit (Dulong-Petit) as well as the model calculation in this work. The irradiated results for specific heat do not show an obvious fission density dependence and are consistent with range of literature data of unirradiated $U_3Si_2$. The model calculation appears to be in the lower range of the distribution of literature values for the specific heat capacity of $U_3Si_2$.

## 4. Discussion

### 4.1. Thermal conductivity

The evolution of thermal conductivity with respect to porosity and fission density has been shown in Figs. 4A and 4B. It is evident that increases in porosity and fission density lead to a decrease in thermal conductivity. This is consistent with the model predictions in this work. As nuclei split due to the fission chain reaction, highly energetic fission fragments are created which lose their energy to the lattice by its electronic stopping power and subsequently by nuclear stopping interactions. The latter phenomenon yields primary knock-on atoms which displace a significant number of lattice atoms through ballistic collisions. As a result, the material accumulates point and extended defects, also known as radiation damage. At sufficiently low temperatures, the ability of certain materials, such as $U_3Si_2$ to accumulate damage in their crystalline form is limited and thus their long-range lattice order is destroyed [27]. This loss in long range order significantly reduces the mean free path of lattice vibrations and, thus, degrades the lattice ther-

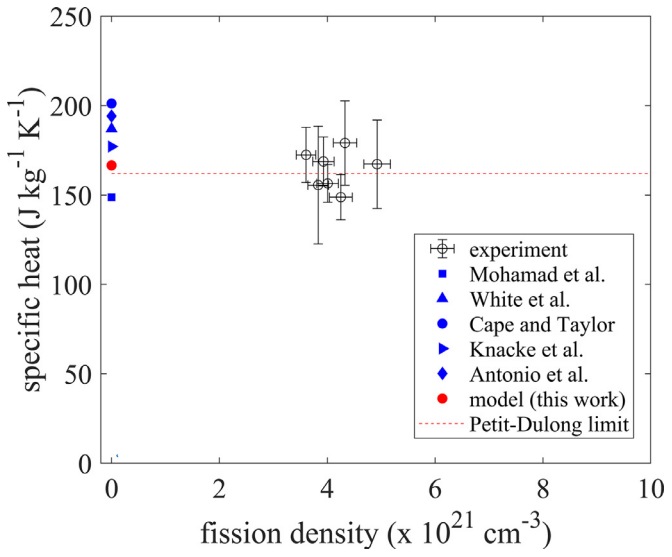


**Fig. 6.** Specific heat of $U_3Si_2$ as a function of fission density. The measured data in this work is compared to the model results, the Dulong-Petit limit as well as various literature data sets - Mohamad, [32] (at 323 K), White, [17](at 320 K), Cape and Taylor [33] (at 300 K), Knacke et al. [34](at 323 K), Antonio, [31] (at 300 K). The fission density is reported per volume of fuel. All errors represent a single standard deviation.

mal conductivity of $U_3Si_2$. In this work it has been estimated the phonon contribution to thermal conductivity of irradiated (amorphous) $U_3Si_2$ has been reduced to 2.175 W $m^{-1}$ $K^{-1}$ which compares favorably with the results of Antonio, et al. [31] (1.99 W $m^{-1}$ $K^{-1}$) and Jossou et al. [35] (2.03 W $m^{-1}$ $K^{-1}$). In addition, the amorphized compound exhibits higher diffusion coefficients and enhanced plasticity due to an increase in the free volume [36]. This results in the enhanced diffusion of fission gas atoms. The amorphous material also exhibits a smaller point defect recombination volume compared to its crystalline state [37,38]. All these phenomena facilitate and enhance the precipitation and growth of fission gas bubbles. These bubbles represent an insulating secondary phase and further enhance the degradation of the material's thermal conductivity. It must be noted that the current analysis has not considered the presence of the USi phase which has been shown to form as fission reduces the U to Si ratio [39]. Furthermore, excess Si is added during fabrication to mitigate the formation of pure uranium precipitates [40] which also favors the formation of USi. USi exhibits a lower thermal conductivity compared to $U_3Si_2$ [41] and lower apparent porosity as a function of burnup (at magnifications and SEM resolutions consistent with the images presented in this work) [39]. Thus, the coexistence of USi and $U_3Si_2$ regions within the fuel particles would introduce variability in the measured thermo-physical property values as a function of burnup and porosity. This is consistent with the scatter observed in the current work's measurements of thermal conductivity, thermal diffusivity and specific heat as a function of both porosity and burnup.

### 4.2. Thermal diffusivity and specific heat

Thermal diffusivity and specific heat results of the irradiated $U_3Si_2$ are shown in Figs. 5 and 6. The specific heat values of irradiated $U_3Si_2$ in this work are consistent with the model prediction and the reported literature values for the unirradiated material. The specific heat of $U_3Si_2$ can be understood in terms of two main physical phenomena – electronic and lattice contributions. The Petit-Dulong limit in Fig. 6 shows the upper limit on the lattice component of specific heat which is a direct result of acoustic phonons reaching their maximum frequency of vibration. The electronic contribution exhibits a second order effect at room temperature. However, as temperature rise the electronic contribution to specific heat is expected to increase as electrons in the conduction band access a greater number of higher energy states. The model prediction for specific heat appears to be in the lower range of the available literature data. This may indicate that the an-harmonic (due to thermal expansion) and defect terms may be significant and should be considered as part of a future study. The thermal diffusivity results for the irradiated material are lower than the unirradiated values obtained from Antonio et al. [31] which is consistent with the model prediction. The evolution of thermal diffusivity with respect to porosity is a consequence of two competing phenomena – an increase resulting from a drop in density and a decrease due to the degradation of thermal conductivity. The latter phenomenon is dominant and, under the assumption of constant specific heat, thermal diffusivity experiences a gradual decrease with increasing porosity. The model tends to overpredict the thermal diffusivity of unirradiated $U_3Si_2$ compared to the value obtained from Antonio et al. [31]. This is consistent with the differences between the model prediction of specific heat in this work and the reported specific heat values in the aforementioned study [31].

### 4.3. Future work

The thermal properties measured in the current study have shown to exhibit a significant uncertainty range. Future studies on irradiated nuclear fuel systems via the TCM will aim to reduce the uncertainties on the measured thermal properties. This will be done by performing a greater number of measurements at each location along the sample surface. Furthermore, future studies would measure and map the local compositional distribution via EDS and EPMA determining the segregation of elements and phases (USi vs $U_3Si_2$ as well as the presence of solid fission product precipitates). These would then inform the thermal conductivity results obtained via the TCM. Finally, a heating stage would be deployed as part of the TCM setup to perform measurements at elevated temperatures.

## 5. Conclusion

This work presents the first direct measurements of thermal conductivity of neutron irradiated $U_3Si_2$ dispersion fuel (most widely used material system for converting research reactor fuel from high to low enrichment). The measurements were performed locally using a state-of-the-art thermo-reflectance technique known as the thermal conductivity microscope or TCM. The local porosity has been estimated via algorithmic analysis of back scattered electron images. A simplified solid-state physics model has been implemented and used to interpret the results. The thermal conductivity has been shown to be significantly lower compared to the fresh material. This degradation is consistent with the presence of fission gas induced porosity and loss of long-range order due to irradiation inflicted amorphization.

## Declaration of Competing Interest

The authors declare that they have no known competing financial interests or personal relationships that could have appeared to influence the work reported in this paper.

## CRediT authorship contribution statement

**T.R. Pavlov:** Conceptualization, Data curation, Formal analysis, Investigation, Methodology, Resources, Software, Validation, Visualization, Writing – original draft. **S.C. Middlemas:** Investigation, Methodology, Visualization, Writing – review & editing. **B.D.**

**Miller:** Methodology, Writing – review & editing. **F. Cappia:** Data curation, Methodology, Writing – review & editing. **J.I. Cole:** Investigation, Funding acquisition, Project administration, Resources, Supervision, Writing – review & editing. **J.J. Giglio:** Investigation, Funding acquisition, Project administration, Resources, Supervision, Writing – review & editing.

## Acknowledgments

This submitted manuscript was authored by a contractor of the U.S. Government under DOE Contract No. DE-AC07-05ID14517. Accordingly, the U.S. Government retains and the publisher, by accepting the article for publication, acknowledges that the U.S. Government retains a nonexclusive, paid-up, irrevocable, worldwide license to publish or reproduce the published form of this manuscript, or allow others to do so, for U.S. Government purposes. The Material Management and Minimization and the Nuclear Science User Facilities programs provided the funding for this work. The authors would like to thank Irina Y. Glagolenko for her expert advice, reading and reviewing the manuscript. Robert S. Schley is thanked for his assistance and expertise regarding the understanding and application of thermo-reflectance techniques. The facility personnel of the Irradiated Materials Characterization Laboratory at INL's Materials and Fuels Complex are thanked for their valuable support.

## Appendix

A1. Thermal conductivity

The thermal conductivity of $U_3Si_2$ can be expressed as a sum of lattice ($k_l$) and electronic ($k_{el}$) terms [25,26]:

$$k_{tot} = k_l + k_{el} \tag{A1}$$

According to the Wiedmann-Franz law the contribution of electrons to the thermal conductivity of a metal are expressed by [30]:

$$k_{el} = L\sigma T \tag{A2}$$

where $L$ is the Lorentz number ($2.44\times10^{-8}$ $W\Omega K^{-2}$), $\sigma$ is the electrical conductivity ($\Omega^{-1}$ $m^{-1}$) and $T$ is temperature (K).

Under irradiation at lower temperatures (below approximately 510 K [15,42]) $U_3Si_2$ becomes amorphous and the lattice component of thermal conductivity reaches its amorphous limit ($k_l = k_{am}$) and hence:

$$k_{tot} = k_{am} + k_{el} \tag{A3}$$

According to Cahill the thermal conductivity limit of an amorphous solid can be expressed by [43,44]:

$$k_{am} = \left(\frac{C_B}{\hbar}\right)^3 \frac{\hbar}{2\pi V} T^2 \int_0^{\frac{\vartheta}{T}} \frac{x^3 e^x}{(e^x-1)^2} dx \tag{A4}$$

where $C_B$ is the Boltzmann constant, $\hbar$ is the reduced Planck constant and the velocity V is expressed via the following relation [45]:

$$V = \frac{C_B \vartheta}{\hbar}\left(\frac{\Omega}{6\pi^2}\right)^{1/3} \tag{A5}$$

where $\Omega$ is the atomic volume ($m^{-3}$). All integrals are performed numerically using the trapezoidal rule.

A2. Specific heat

The molar specific heat of $U_3Si_2$ at room temperature can be expressed by the sum of lattice/harmonic ($c_V^h$) and electronic ($c_V^{el}$) terms [29,30]:

$$c_P^{tot} = c_V^h + c_V^{el} \tag{A6}$$

The component of specific heat due to electrons can be derived from the total electronic internal energy ($U$). This energy can be expressed as the probability of finding an electron at a particular energy ($f(E)$), the electron energy ($E$), and their density of states ($\frac{dN}{dE}$):

$$U = \int_0^\infty \left(E * f(E) * \frac{dN}{dE}\right) dE \tag{A7}$$

The density of states can be described the following Eq. [46]:

$$\frac{dN}{dE} = \left(\frac{2m^*}{\hbar^2}\right)^{\frac{3}{2}} \frac{\sqrt{E}}{2\pi^2} \tag{A8}$$

where $m^*$ is the effective electron mass (kg). The Fermi-Dirac distribution is expressed by the formula below [47]:

$$f(E) = \frac{1}{exp\left(\frac{E-E_f}{C_B T}\right)+1} \tag{A9}$$

where $E_f$ is the Fermi level (eV). By evaluating the integral in Eq. (A7) numerically and taking the numerical derivative with respect to temperature, it is possible to calculate the specific heat at constant volume:

$$c_V^{el} = \frac{dU}{dT} \tag{A10}$$

The specific heat contribution due to lattice vibrations or phonons can be expressed via the Debye integral [25]:

$$c_V^h = 3N_{atoms}C_B\left(\frac{T}{\vartheta}\right)^3 \int_0^{\frac{\vartheta}{T}} \frac{x^4 e^x}{(e^x-1)^2} dx \tag{A11}$$

where $N_{atoms}$ is the number of atoms per molecule of the compound.

## References

[1] D. Keiser, Observed changes in as-fabricated U-10Mo monolithic fuel microstructures after irradiation in the advanced test reactor, JOM 69 (2017) 2538–2545.
[2] D.D. Keiser, S.L. Hayes, M.K. Meyer, C.R Clark, Fuel for nuclear research reactors, Jom 55 (2003) 55–58.
[3] J.L. Snelgrove, G.L. Hofman, M.K. Meyer, C.L. Trybus, T.C Wiencek, Development of very-high-density low-enriched-uranium fuels, Nucl. Eng. Des. 178 (1997) 119–126.
[4] G.L. Hofman, L.C. Walters, T.H Bauer, Metallic fast reactor fuels, Prog. Nucl. Energy 31 (1997) 83–110.
[5] J. Durand, P. Laudamy, K. Richter. *Preliminary developments of MTR plates with uranium nitride*. (1997).
[6] J.M. Beeston, R.R. Hobbins, G.W. Gibson, W.C. Francis, Development and irradiation performance of uranium aluminide fuels in test reactors, Nucl. Technol. 49 (1980) 136–149.
[7] L.S Castleman, Layer growth during interdifusion in the aluminum-uranium alloy system, J. Nucl. Mater 3 (1961) 1–15.
[8] S.H. Lee, J.M. Park, C.K Kim, Thermophysical properties of U-Mo/Al alloy dispersion fuel meats, Int. J. Thermophys. 28 (2007) 1578–1594.
[9] J. Rest, G.L. Hofman, Y.S Kim, Analysis of intergranular fission-gas bubble-size distributions in irradiated uranium-molybdenum alloy fuel, J. Nucl. Mater 385 (2009) 563–571.
[10] Y.S. Kim, G.L Hofman, Interdiffusion in U3Si-Al, U3Si2-Al, and USi-Al dispersion fuels during irradiation, J. Nucl. Mater 410 (2011) 1–9.
[11] S. Nazare. *International meeting on reduced enrichment for research and test reactors* A comparison of the metallurgical behaviour of dispersion fuels with uranium silicides and U6Fe as dispersants. in 85-94 (1984).
[12] M. Ugajin, M. Akabori, A. Itoh, N. Ooka, Y Nakakura, Behavior of neutron-irradiated U 3Si, J. Nucl. Mater 248 (1997) 204–208.
[13] G.L Hofman, Crystal structure stability and fission gas swelling in intermetallic uranium compounds, J. Nucl. Mater 140 (1986) 256–263.
[14] Y.S. Kim, G.L. Hofman, J. Rest, A.B. Robinson, Temperature and dose dependence of fission-gas-bubble swelling in U3Si2, J. Nucl. Mater. 389 (2009) 443–449.
[15] Y.S. Kim, Comprehensive Nuclear Materials Uranium intermetallic fuels, Elsevier Inc., 2012 *(U-Al,U-Si, U-Mo)*. **3**.
[16] G.L. Hofman, L.A. Neimark, *Reduced enrichment for research and test reactors:* Postirradiation analysis of experimental uranium-silicide dispersion fuel plates. in 75-85 (1985).
[17] J.T. White, Thermophysical properties of U3Si2 to 1773 K, J. Nucl. Mater. 464 (2015) 275–280.

[18] Z. Hua, Spatially localized measurement of thermal conductivity using a hybrid photothermal technique, J. Appl. Phys. 111 (2012) 1–7.
[19] S. Middlemas, Determining local thermal transport in a composite uranium-nitride/silicide nuclear fuel using square-pulse transient thermoreflectance technique, J. Nucl. Mater. 528 (2020) 1–11.
[20] C.A. Adkins, Demonstrate Thermal Property Measurement on Irradiated Fuel in IMCL, 2019.
[21] D.M. Perez, RERTR-8 Irradiation Summary Report, 2011.
[22] D.D. Keiser, The use of U3Si2/Al dispersion fuel for high power research reactors, J. Nucl. Mater 528 (2020) 151820.
[23] D. Hurley, R. Schley, *Enter TCM and Associated Equipment into Stage One Mockup*. (2017).
[24] J. Pakarinen, Microstructure changes and thermal conductivity reduction in UO2 following 3.9 MeV He2+ ion irradiation, J. Nucl. Mater. 454 (2014) 283–289.
[25] T.R. Pavlov, Measurement and interpretation of the thermo-physical properties of $UO_2$ at high temperatures: the viral effect of oxygen defects, Acta Mater (2017) 139.
[26] T.R. Pavlov, Examining the thermal properties of unirradiated nuclear grade graphite between 750 and 2500 K, J. Nucl. Mater. 538 (2020) 152176.
[27] T. Yao, *Mater.* Radiation-induced grain subdivision and bubble formation in U3Si2 at LWR temperature, J. Nucl. 498 (2018) 169–175.
[28] L. Gong, Y. Wang, X. Cheng, R. Zhang, H Zhang, Thermal conductivity of highly porous mullite materials, Int. J. Heat Mass Transf 67 (2013) 253–259.
[29] T.R. Pavlov, *Sci. Rep.* High temperature measurements and condensed matter analysis of the thermo-physical properties of $ThO_2$. **8**, (2018).
[30] T. Pavlov, A new numerical method and modified apparatus for the simultaneous evaluation of thermo-physical properties above 1500 K: A case study on isostatically pressed graphite, Thermochim. Acta 652 (2017).
[31] D.J. Antonio, Thermal and transport properties of U3Si2, J. Nucl. Mater. 508 (2018) 154–158.
[32] A. Mohamad, Y. Ohishi, H. Muta, K. Kurosaki, S. Yamanaka, Thermal and mechanical properties of polycrystalline U3Si2 synthesized by spark plasma sintering, J. Nucl. Sci. Technol. 55 (2018) 1141–1150.
[33] J. Cape, R. Taylor. *Thermal Properties of Refractory Materials*. (1961).
[34] I. Barin, O. Knacke, O. Kubaschewski. Thermochemical properties of inorganic Compounds. 783 (1977).
[35] E. Jossou, Anisotropic thermophysical properties of U3Si2 fuel: an atomic scale study, J. Nucl. Mater. 521 (2019) 1–12.
[36] G.L. Hofman, Y.S Kim, A classification of uniquely different types of nuclear fission gas behavior, *Nucl. Eng. Technol* 37 (2005) 299–308.
[37] A. Audouard, J. Balogh, J. Dural, J.C. Jousset, Displacement threshold energy of iron atoms in amorphous and crystalline Fe75B25 alloys, Radiat. Eff. 62 (1982) 161–165.
[38] J Rest, A generalized model for radiation-induced amorphization and crystallization of U3Si and U3Si2 and recrystallization of UO2, J. Nucl. Mater 240 (1997) 205–214.
[39] A. Leenaers, E. Koonen, Y. Parthoens, P. Lemoine, S Van den Berghe, Post-irradiation examination of AlFeNi cladded U3Si2 fuel plates irradiated under severe conditions, J. Nucl. Mater 375 (2008) 243–251.
[40] A. Leenaers, J. Wight, S. Van den Berghe, H.J. Ryu, J.-F. Valery, *Comprehensive Nuclear Materials* U-Si Based Fuel System, 2020 485-498, doi:10.1016/b978-0-12-803581-8.11607-8.
[41] J.T. White, A.T. Nelson, J.T. Dunwoody, D.D. Byler, K.J McClellan, Thermophysical properties of USi to 1673 K, J. Nucl. Mater 471 (2016) 129–135.
[42] Y. Miao, In-situ TEM ion irradiation investigations on U3Si2 at LWR temperatures, J. Nucl. Mater 484 (2017) 168–173.
[43] D.G. Cahill, S.K. Watson, R.O Pohl, Lower limit to the thermal conductivity of disordered crystals, Phys. Rev. B 46 (1992) 6131–6140.
[44] D.G. Cahill, R.O Pohl, Heat flow and lattice vibrations in glasses, Solid State Commun 70 (1989) 927–930.
[45] T.R. Pavlov, Experimental Determination and Modelling of Various Thermo–Physical Properties of Nuclear Materials Above 1500K, Imperial College London, 2018.
[46] H. Ibach, H. Lüth. *Solid-State Physics: An Introduction to Principles of Materials Science*. (2003).
[47] W.W. Chow, S.W. Koch. *Semiconductor-Laser Fundamentals: Physics of the Gain Materials*. (1999).